

National Institute of Standards and Technology) filter nomograph that aids in the selection of the best filter for a given light source and color photographic emulsion. The filters suggested may not be exact for accurate color reproduction, but will always be close enough to enable intelligent changes for achieving accuracy. A comparison of several color films has shown that differences in contrast and color rendition occur (Ref 51).

Digital techniques involve digital processing of an analog signal or the more direct digitization of an image with solid-state camera. Cameras are mounted with C-mounts or a bayonet attachment. The C-mount will allow the image to be focused at the plane of the sensors in the camera. The image is focused through the eyepiece and then the object in the preview screen is made sharp and crisp by adjusting the C-mount. Good lighting and the correct microscope optics are still required to acquire a good image, just as in image acquisition on film.

Solid-state cameras employ charge-coupled or charge-injected devices, which are a matrix of small, accurately spaced photosensitive elements. When light passing through the camera lens strikes the array, each detector converts the light falling on it into a corresponding analog electrical signal. The entire image is thus broken down into an array of individual picture elements, or pixels. The magnitude of the analog voltage for each pixel is directly proportional to the intensity of light in that portion of the image. Charge-coupled and charge-injected device arrays differ primarily in how the voltages are extracted from the sensors.

The voltage from each pixel represents an average of the light-intensity variation on the area of the individual pixel. Incident light photons are converted into an analog voltage, which is then digitized into gray scale based on the intensity of light. Cameras may have an analog to digital converter (A/D) of 8 bits yielding 2^8 (256) levels, 14 bits giving 2^{14} (16,384) levels, or 16 bits 2^{16} (65,536) levels, and so on. Most commercial digital cameras offer at least 256 (2^8) gray levels, although there are 12-bit and 16-bit cameras. Naturally, the more levels available, the greater the sensitivity to subtle changes in the incident light. Color is captured in some cameras by having sets of pixels where each pixel samples a specific primary color. For microscopy, most cameras use filters and all the pixels give information on each of the three primary colors. For the 8-bit A/D, $256 \times 256 \times 256 = 16,777,216$ color variations can be assigned.

The necessary resolution and memory depend on contrast resolution (sensitivity) and spatial resolution requirements. In terms of contrast sensitivity (or dynamic range), the human eye can differentiate only 40 gray levels. However, because the human eye can discern several thousand shades of color, assigning individual shades of color to more than 250 gray levels can significantly increase the amount of information recognizable in an image. In addition, computerized image-analysis (IA) systems allow for gray-image processing and transformations. However, it is considered prudent to use gray-

image processing as a last resort for metallographic specimens. Different etches and filters (other than the standard green filter) should be evaluated prior to gray-scale transformations (Ref 53).

Sufficient spatial resolution of the detector must also be compatible with the microscope. In microscopy with visible light, for example, the theoretical limit at which it is no longer possible to distinguish two adjacent lines is about $0.2 \mu\text{m}$ (or about $0.3 \mu\text{m}$ for dry objectives). The theoretical expression for optical resolution (d) of a light microscope is:

$$d = \frac{1.22 \times \lambda}{2 \cdot NA}$$

where λ is the wavelength of light (approximately $0.55 \mu\text{m}$). In order to properly match resolution of the detector with that of the microscope, it is necessary to know the number of detectors and their size relative to the image projected onto the array surface by the microscope. Thus, required pixel size depends on the optical resolution (d), the objective magnification, and any additional zoom (commonly $2.5 \times$ zoom on many metallurgical microscopes). For a given optical resolution (d), required pixel size is larger as the objective magnification is increased (e.g., see Table 2 and Fig. 46). Conversely, required pixel size becomes smaller when optical resolution is increased at a given objective magnification (e.g., Table 2 and Fig. 46). In addition, smaller pixels and a larger array size are required when a larger area is recorded by the CCD after zooming into a field of view at a given NA setting and objective magnification (compare Fig. 46a with 46c and compare Fig. 46b with 46d).

Currently available CCD arrays vary in size from several hundred to many thousands of pixels. Modern array sizes used in devices intended for scientific investigations range from 1000×1000 up to 5000×5000 sensor elements. The trend in consumer- and scientific-grade CCD manufacture is for the sensor size to continuously decrease, and digital cameras with photodiodes as small as $4 \times 4 \mu\text{m}$ are currently available. Typical solid-state cameras have arrays ranging from 1×10^6 pixels (1024×1024 pixel array) to 4×10^6 pixels. In an average 35-mm silver halide film, there are about 20×10^6 pixels. The trend is to reduce the size of the photodetector for each pixel, but reducing pixel size can reduce dynamic range, or contrast sensitivity, of the pixel.

The determination of adequate pixel arrays for a given application also influences the sampling necessary to achieve adequate statistical relevance and the necessary revolving power to obtain accurate measurements. For example, if it is possible to resolve the features of interest using the same microscope setup and two cameras having differing resolutions, the camera having the lowest resolution should be used because it will cover a much greater area of the sample (Ref 56). The following is an example (Ref 56).

Consider a system using a $16 \times$ objective and a 1024×1024 resolution camera, each pixel is $0.3 \mu\text{m}^2$. Measuring 10 fields to provide sufficient sampling statistics provides a total area of 0.94 mm^2 (0.001 in.^2). Using the same objective, but switching to a 760×574 pixel camera, the pixel size is $0.66 \mu\text{m}^2$. To measure the same total area of 0.94 mm^2 , it would only require the measurement of five fields. This could save substantial time if the analysis is complicated and slow, or if there are hundreds or thousands of samples to measure (assuming that it is possible to sufficiently resolve features of interest using either camera and the same optical setup, which often is not the case).

The key point is whether or not the features of interest can be sufficiently resolved. Additional information on processing, compression, and analysis of digital images are discussed in the articles, "Digital Imaging" and "Quantitative Image Analysis" in this Volume.

Macrophotography

Examination and photography are often required for such objects as macroetched disks and broken parts. Examination can be performed visually or with the aid of a simple hand lens or stereomicroscope. Macrophotography can be performed using most cameras, perhaps aided by the use of close-up lens attachments, a bellows, or a macrolens. Stereomicroscopes are useful for macroexamination and can be used in preliminary examinations to point out specific features for more detailed study. Digital stereomicroscopes (Fig. 47) are capable of high-resolution photography or high-speed video for time-sensitive applications. Some will take stereopairs. A few manufacturers offer camera stands for macrophotography. Some metallographs also have low-magnification objectives that can perform certain types of macrophotography.

Table 2 Objective resolution and theoretical size of the CCD cell

Objective magnification	Numerical aperture	Objective resolution, μm	Theoretical cell size, μm	Number of cells per 22 mm
$4 \times$	0.10	3.36	13.4	1642
$10 \times$	0.25	1.34	13.4	1642
$20 \times$	0.40	0.84	16.8	1310
$40 \times$	0.65	0.52	20.6	1068
$60 \times$	0.95	0.35	21.2	1038
$60 \times$, oil	1.40	0.24	14.4	1528
$100 \times$, oil	1.40	0.24	24.0	917

CCD, charge-coupled device. Source: Ref 54

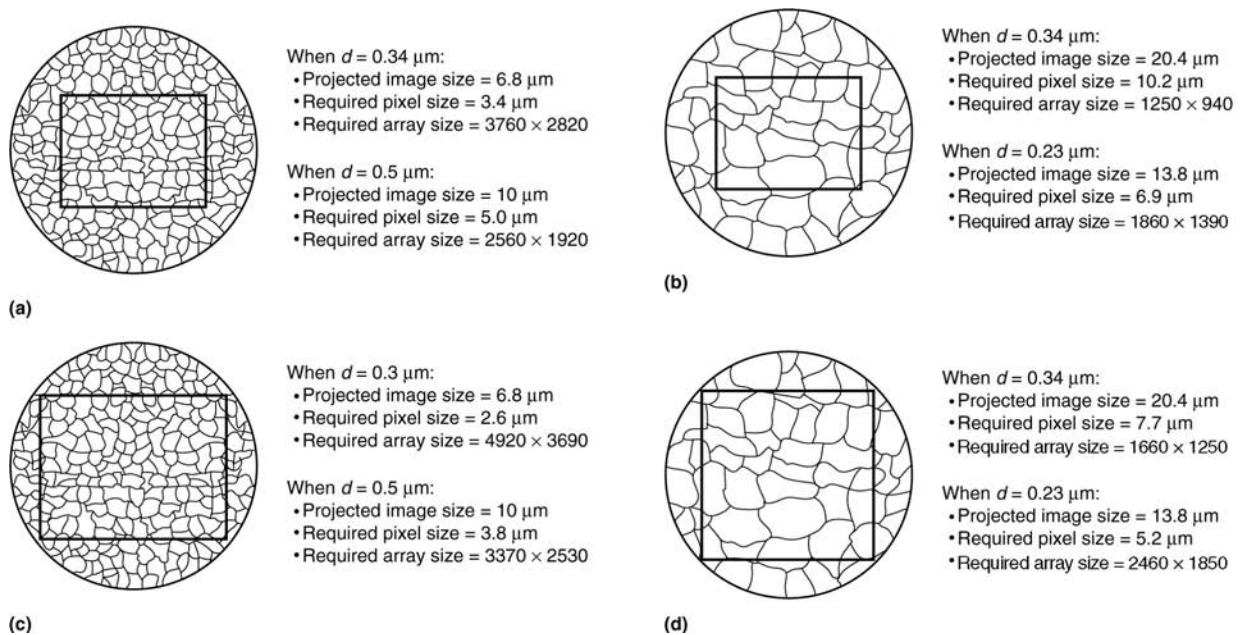


Fig. 46 Pixel requirements for a 12.8×9.6 mm CCD array (size not shown to scale) to match the optical resolution (d) and objective magnification of a microscope. (a) $20\times$ objective magnification without zoom. (b) $60\times$ objective magnification without zoom. (c) $20\times$ objective magnification with 0.75 zoom. (d) $60\times$ objective magnification with 0.75 zoom. Adapted from Ref 55

Macrophotography utilizes magnifications from less than $1\times$ to $50\times$. Most laboratories, especially those engaged in failure analyses, have various cameras, light sources, and stereoviewers to cover the wide range of objects photographed. Correct lighting is necessary to emphasize details and provide even illumination without glare or reflection. Adjustment of lighting requires some experimentation and experience. Available lighting includes flood lamps,

rings, coaxial, or fiber optics. A light box is useful for eliminating shadows, but considerable creativity is required to obtain good results.

Depth of field and resolution are important variables. Many of the objects to be photographed are three-dimensional, which requires a certain depth of field and proper lighting to reveal shape and texture. Depth of field varies with the aperture diaphragm lens setting, the magnification, and the focal length of the lens. Stopping down the aperture improves depth of field, but decreases image brightness and clarity. Depth of field also increases as magnification decreases and focal length increases. Depth of field can be estimated by:

$$\text{Depth of field} = 2(f\text{-number})(C)[1 + 1/M] \quad (\text{Eq 6})$$

where depth of field is in mm, C is the circle of confusion of the subject ($0.33/M$), and M is the magnification. Long-focal-length lenses are preferred for macrophotography to avoid distortion and astigmatism. For magnifications below $5\times$, focal lengths of 100 mm or more are preferred. Shorter-focal-length lenses are used for higher magnifications. Additional details concerning macrophotography can be found in Ref 57 to 60.

REFERENCES

1. R.C. Gifkins, *Optical Microscopy of Metals*, American Elsevier, 1970
2. R.P. Loveland, *Photomicrography: A Comprehensive Treatise*, Vol 1 and 2, John Wiley & Sons, 1970
3. V.A. Phillips, *Modern Metallographic Techniques and Their Applications*, Interscience, 1971

4. J.H. Richardson, *Optical Microscopy for the Materials Sciences*, Marcel Dekker, 1971
5. H.W. Zieler, *The Optical Performance of the Light Microscope*, Microscope Publications Ltd., Part 1, 1972, Part 2, 1974
6. R.B. McLaughlin, *Accessories for the Light Microscope*, Microscope Publications, Ltd., 1975
7. R.B. McLaughlin, *Special Methods in Light Microscopy*, Microscope Publications, Ltd., 1977
8. H. Modin and S. Modin, *Metallurgical Microscopy*, Halsted Press, John Wiley & Sons, 1973
9. G.F. Vander Voort, *Metallography: Principles and Practice*, McGraw-Hill, 1984
10. K.-H. Schade, *Light Microscopy—Technology and Application*, 3rd ed., Verlag Moderne Industrie, 2001
11. H.W. Zieler, What Resolving Power Formula Do You Use? *Microscope*, Vol 17, 1969, p 249–270
12. C. Van Duijn, Visibility and Resolution of Microscopic Detail, *Microscope*, Vol 11, 1957, p 196–208
13. G.K. Conn and F.J. Bradshaw, Ed., *Polarized Light in Metallography*, Butterworths, 1952
14. W.C. McCrone et al., *Polarized Light Microscopy*, Ann Arbor Science Publishers, 1978
15. A.F. Hallimond, *The Polarizing Microscope*, 3rd ed., Vickers Instruments, 1970
16. E.C.W. Perryman and J.M. Lack, Examination of Metals by Polarized Light, *Nature*, Vol 167 (No. 4247), 1951, p 479
17. A.H. Bennett et al., *Phase Microscopy*, John Wiley & Sons, 1951



Fig. 47 Digital stereomicroscope with trinocular head allowing attachment of any C-mount compatible still or video camera. Courtesy of Olympus Corporation of America

18. C.E. Price, Differential Interference Contrast, *Metallography and Microstructures*, Vol 9, *ASM Handbook*, American Society for Metals, 1985, p 150–152
19. J. Padawer, The Nomarski Interference-Contrast Microscope: An Experimental Basis for Image Interpretation, *J. R. Microsc. Soc.*, Vol 88 (Part 3), 1968, p 305–349
20. R. Hoffman and L. Gross, Reflected-Light Differential-Interference Microscopy: Principles, Use and Image Interpretation, *J. Microsc.*, Vol 91 (Part 3), 1970, p 149–172
21. A.S. Holik, Surface Characterization by Interference Microscopy, *Microstruct. Sci.*, Vol 3B, 1975, p 991–1010
22. M. Francon and T. Yamamoto, A New and Very Simple Interference System Applicable to the Microscope, *Optica Acta*, Vol 9, 1962, p 395–408
23. M.G. Nomarski, Microinterférométrie Différentiel à Ondes Polarisées, *J. Phys. Radium*, Vol 16, 1955, p 9
24. M.G. Nomarski and A.R. Weill, Application à la Métallographie des Méthodes Interférentielles à Deux Ondes Polarisées, *Revue de Metall.*, Vol 52, 1955, p 121–134
25. F. Herzog, Polarization Interferometric Methods in Incident-light Microscopy, with Special Reference to Material Testing, *Ind. Anz.*, Vol 60, July 1962, p 27–31
26. M. Francon and S. Mallick, *Polarization Interferometers*, Wiley-Interscience, 1975
27. W. Lang, “Nomarski Differential Interference Contrast Microscopy, Part IV: Applications,” *Zeiss Information*, No. 77/78, 1971, p 22–26
28. S. Tolansky, *Multiple-Beam Interferometry of Surface and Films*, Clarendon Press, 1948
29. S. Tolansky, *Surface Microtopography*, Interscience, 1960
30. A.M.A. Schmidt and R. D. Compton, Confocal Microscopy, *Friction, Lubrication, and Wear Technology*, Vol 18, *ASM Handbook*, ASM International, 1992, p 357–361
31. M.G. Lozinskii, *High Temperature Metallography*, Pergamon Press, 1961
32. B.L. Bramfitt et al., The Use of Hot-Stage Microscopy in the Study of Phase Transformations, in *Metallography—A Practical Tool for Correlating the Structure and Properties of Materials*, STP 557, ASTM, 1974, p 43–70
33. K.A. Jackson and J.D. Hunt, Transparent Compounds That Freeze Like Metals, *Acta Metall.*, Vol 3, 1965, p 1212–1215
34. P. Tardy, New Methods for Direct Observation of the Recrystallization of Low Melting Metals, *Pract. Metallog.*, Vol 9, 1968, p 485–493
35. M. Markworth, Preparation of Metallographic Specimens of Ferrous Materials by Electrolytic Polish Attack under Direct Microscope Observation, *Neue Hütte*, Vol 13 (No. 11), 1968, p 684–689
36. R. Wall and D.I. Roberts, A Cell Technique for Microscopic Observation of Selective Corrosion, *Metallurgia*, Vol 68 (No. 410), 1963, p 291–294
37. R.A. Flinn and P.K. Trojan, Examination of Microstructures under Varying Stress, *Met. Prog.*, Vol 68, July 1955, p 88–89
38. E. Brobery and R. Attermo, A Miniature Tensile-Testing Machine for Deformation During Microscopic Observation, *Jernkontorets Ann.*, Vol 152 (No. 10), 1968, p 525–526
39. D. Godfrey, “Investigation of Fretting by Microscopic Observation,” Report 1009, National Advisory Committee for Aeronautics, 1951
40. J.L. Walter and H.E. Cline, Grain Boundary Sliding, Migration, and Deformation in High-Purity Aluminum, *Trans. AIME*, Vol 242, 1968, p 1823–1830
41. S. Takeuchi and T. Homma, Direct Observation for High Temperature Fatigue in Pure Metals by Means of Microscopic Cine-Camera, *Proc. First International Conference on Fracture* (Sendai, Japan), Vol 2, 1966, p 1071–1086
42. G.L. Kehl et al., The Removal of Inclusions for Analysis by an Ultrasonic “Jack Hammer” *Metallurgia*, Vol 55, March 1957, p 151–154
43. J.H. Evans, Remote Metallography, in *Interpretive Techniques for Microstructural Analysis*, Plenum Press, 1977, p 145–168
44. R.J. Gray et al., Metallography of Radioactive Materials at Oak Ridge National Laboratory, *Applications of Modern Metallographic Techniques*, STP 480, ASTM, 1970, p 67–96
45. L. Koscec and F. Vodopivec, Examples of the Replica Technique in Optical Metallography, *Pract. Metallog.*, Vol 6, 1969, p 118–121
46. J. Neri, Optical Replicas—A Nondestructive Metallographic Evaluation Technique, in *Failure Analysis*, American Society for Metals, 1969, p 241–268
47. *Photomicrography of Metals*, Kodak Scientific Publication P-39, 1971
48. *Photography through the Microscope*, Kodak Scientific Publication P-2, 1980
49. L.E. Samuels, Photographic Methods, in *Interpretive Techniques for Microstructural Analysis*, Plenum Press, 1977, p 17–42
50. B.H. Carroll et al., *Introduction to Photographic Theory*, John Wiley & Sons, 1980
51. R.S. Crouse, R.J. Gray, and B.C. Leslie, Applications of Color in Metallography and Photography, *Interpretive Techniques for Microstructural Analysis*, J.L. McCall and P.M. French, Ed., Plenum Press, 1977 p 43–64
52. H.E. Exner et al., Some Experiences in the Documentation of Colour Micrographs, *Pract. Metallog.*, Vol 17, 1980, p 344–351
53. D. Hetzner, Chapter 8 Applications, *Practical Guide to Image Analysis*, ASM International, 2000, p 204
54. L. Wojnar and K. Kurzydowski, Chapter 7, Analysis and Interpretation, *Practical Guide to Image Analysis*, ASM International, 2000, p 172
55. <http://www.microscopyu.com/tutorials/java/pixelcalculator/>, Nikon MicroscopyU, Jan 2004
56. J.C. Grande, Chapter 4, Principles of Image Analysis, *Practical Guide to Image Analysis*, ASM International, 2000, p 78
57. *Simplified Photomacrography*, Kodak Scientific Publication P-53, 1970
58. *Photomacrography*, Kodak Technical Publication N-12B, 1972
59. J.R. Dvorak, Photomacrography in Metallography, *Microstruc. Sci.*, Vol 3B, 1975, p 1011–1025
60. *Photomacrography and Photomicrography*, Wild Heerbrugg, Ltd., Switzerland, 1979



Fig. 14 Mechanically twinned hafnium weld. Specimen was attack polished and heat tinted (~400 °C, or 750 °F). Polarized light illumination. 60×. (P.E. Danielson)

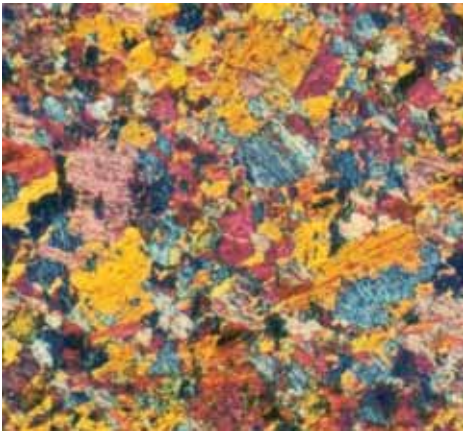


Fig. 16 Color etching (10% aqueous $\text{Na}_2\text{S}_2\text{O}_5$) revealed the lath martensite packet size of AF 1410 ultrahigh-strength steel that was heat treated (austenitized at 900 °C, or 1650 °F, water quenched, and tempered at 675 °C, or 1250 °F). Polarized light illumination. 100×. (G.F. Vander Voort)

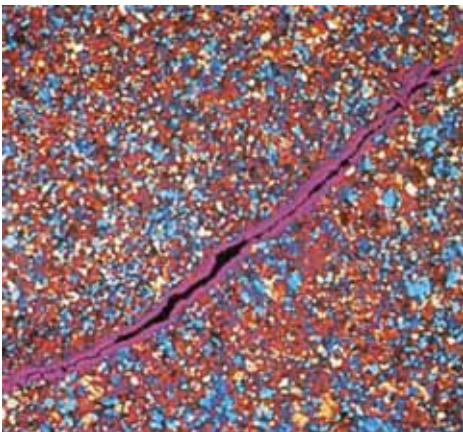
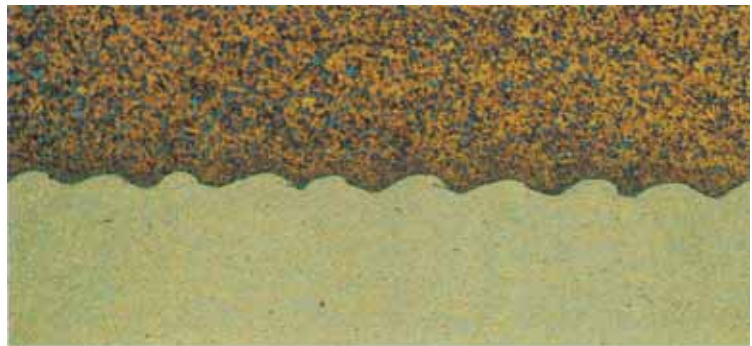
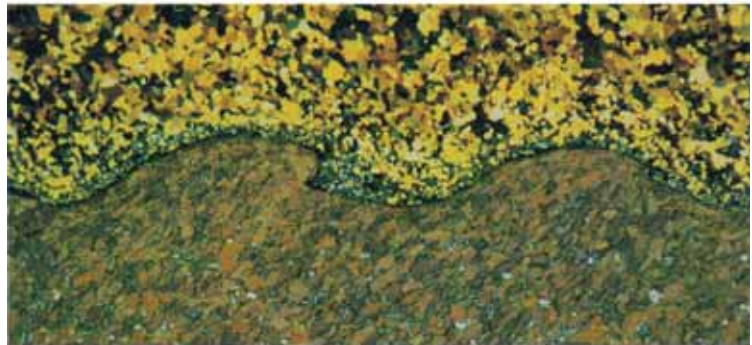


Fig. 17 Recrystallized Ti-6Al-4V alloy with a crack resulting from creep-rupture testing. Attack polished and color etched in 100 mL distilled H_2O , 4 mL HCl, and 3 g NH_4HF_2 . Polarized light illumination. 100×. (G. Müller)



(a)



(b)

Fig. 15 Explosive-bonded 3.2 mm ($\frac{1}{8}$ in.) thick zirconium clad to 32 mm ($1\frac{1}{4}$ in.) thick carbon steel plate. Attack polished, swab etched with 97% methanol and 3% HNO_3 , and heat tinted at 370 °C (700 °F). (a) Under bright-field illumination, the zirconium is brown-blue and shows some grain orientation. The steel is yellow-green. 15×. (b) Note the difference between the anisotropic zirconium (top) and the isotropic steel (bottom) under polarized light illumination. 85×. (P.E. Danielson)



Fig. 18 Ti-6Al-4V alloy containing martensite needles formed at elevated temperature (>840 °C, or 1540 °F). Color etched in 100 mL H_2O , 4 mL HCl, 3 g NH_4HF_2 . Polarized light illumination. 100 \times . (G. Müller)

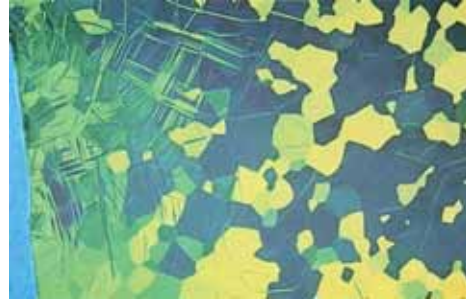
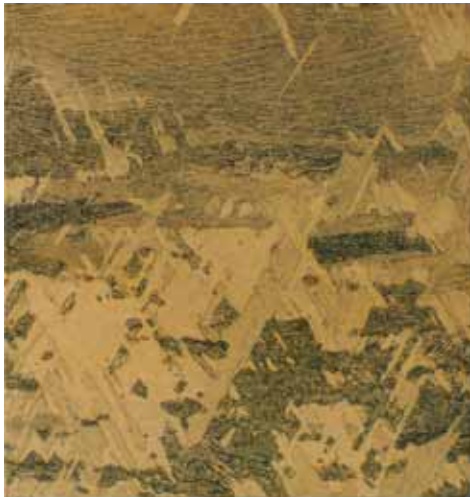


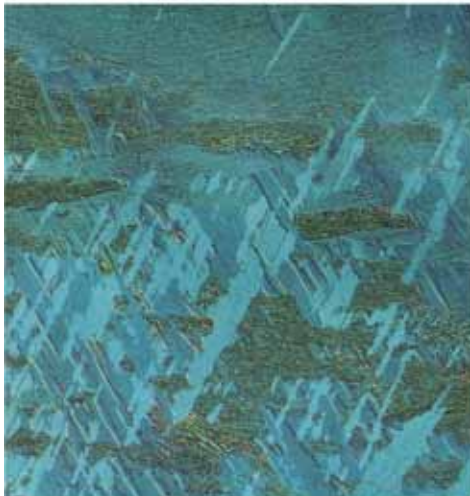
Fig. 19 Titanium alloy with a zone of mechanical deformation caused during shearing the specimen from an 8 mm (0.3 in.) diameter bar. The light-blue area on the side is mounting resin. Attack polished. Polarized light illumination. 200 \times . (G. Müller)



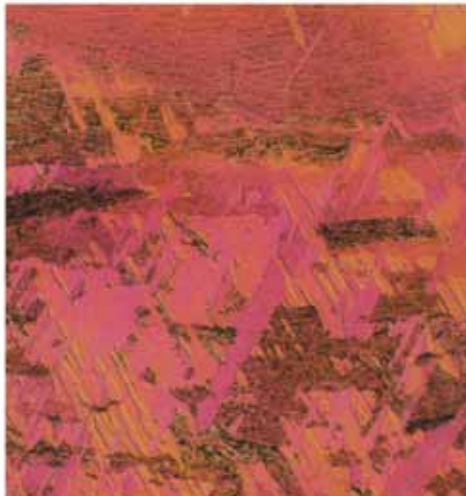
(a)



(b)



(c)



(d)

Fig. 20 Comparison of bright-field illumination (a), cross-polarized light (b), and differential interference contrast illumination (c and d) used to examine the basketweave pattern of an α - β Ti-6Al-4V alloy. Figures (c) and (d) illustrate the observation of reversed topography by adjusting the Wollaston prism. The same effect can be seen in Fig. 22. Kroll's reagent. 200 \times . (G.F. Vander Voort)

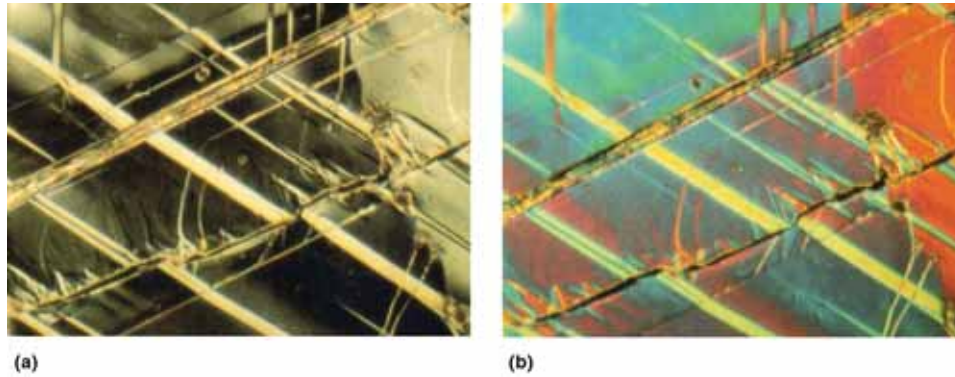


Fig. 21 As-cleaved antimony specimen viewed under differential interference contrast illumination. Views under different contrast conditions show the greater sensitivity in the gray regime (a) than in the nongray regime (b). Twins, river patterns, and cracks are present. As-polished. $200\times$. (C.E. Price)

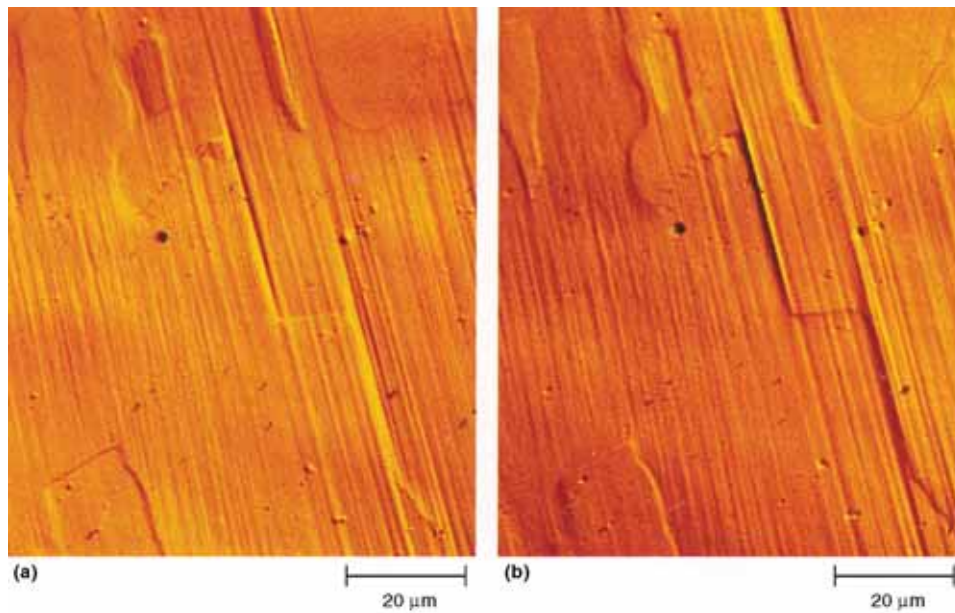


Fig. 22 Plastically deformed Nickel 200 specimen viewed under orange differential interference contrast illumination to either side of the Wollaston prism symmetry position so that the height differences appear reversed. Chemically polished. $800\times$. (C.E. Price). See also Fig. 35 in the article "Light Microscopy."



Fig. 23 Hafnium crystal bar showing twins caused by cold working. Attack polished, heat tinted at 480 °C (900 °F), and viewed under differential interference contrast illumination. 65×. (P.E. Danielson)

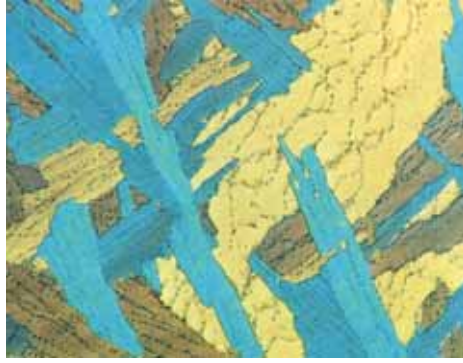


Fig. 24 Zircaloy 4 as-cast ingot. Use of attack polishing, heat tinting (425 °C, or 800 °F), and differential interference contrast illumination reveals the basic crystal structure and the iron-chromium second phase. 200×. (P.E. Danielson)

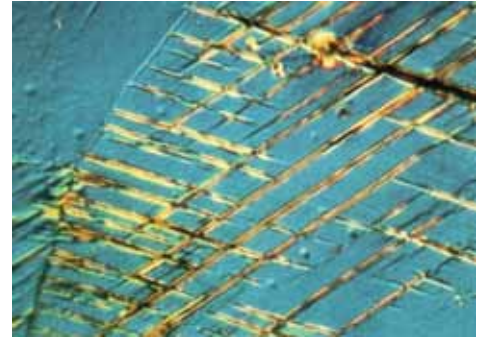


Fig. 25 Nickel 200 specimen fatigued in reverse bending for 10⁴ cycles. Use of differential interference contrast illumination shows persistent slip bands with associated cracks outlined against a blue background. Chemically polished. 800×. (C.E. Price)



Fig. 26 Zircaloy forging as viewed under differential interference contrast illumination. The parallel platelet structure is an area lower in carbon content. Etched in 45 mL H₂O, 45 mL HNO₃, and 10 mL HF and heat tinted at 425 °C (800 °F). 100×. (P.E. Danielson)

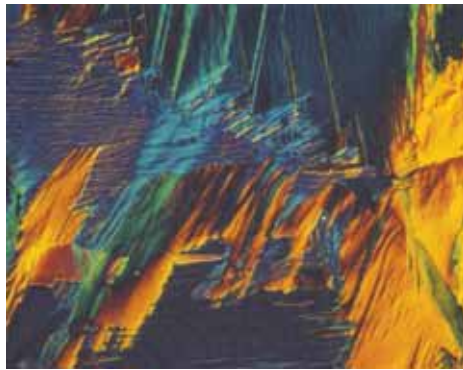


Fig. 27 As-cast Zircaloy structure as viewed under differential interference contrast illumination. The high mechanical deformation evident was induced deliberately during specimen preparation. Attack polished and heat tinted at 425 °C (800 °F). 100×. (P.E. Danielson)

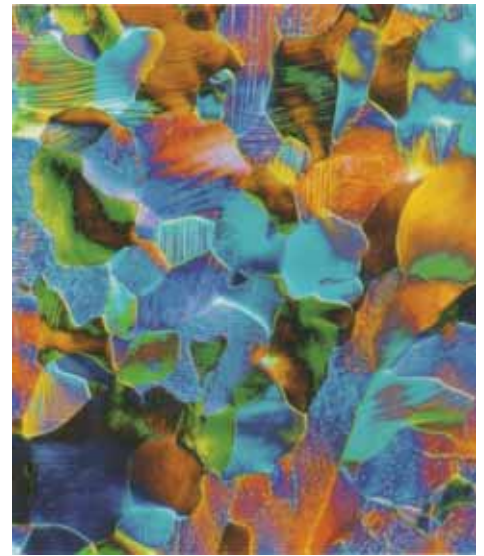


Fig. 28 Heat-tinted niobium alloy (C103) plate as viewed under differential interference contrast illumination. Some of the grains exhibit a second phase (note small, particle-like features) due to alloying additions. 65×. (P.E. Danielson)

Scanning Electron Microscopy

H.E. Exner and S. Weinbruch, Darmstadt University of Technology

THE SCANNING ELECTRON MICROSCOPE is one of the most versatile instruments for investigating the microstructure of materials. Under electron bombardment, a variety of different signals is generated (including secondary electrons, backscattered electrons, characteristic x-rays, and long-wave radiation in the ultraviolet and visible region of the spectrum) that can be used for materials characterization. Using secondary electrons, scanning electron microscopy (SEM) expands the resolution range to a few nanometers (under favorable conditions), thus bridging the gap between optical (light) microscopy and transmission electron microscopy. In addition to the higher lateral resolution, SEM also has a much greater depth of field compared to optical microscopy, due to the small size of the final lens aperture and the small working distance. Scanning electron microscopy offers possibilities for image formation that are usually easy to interpret and will reveal clear pictures of as-polished and etched cross sections as well as rough surfaces and particles. Energy-dispersive x-ray microanalysis using equipment routinely attached to the scanning electron microscope features qualitative and quantitative analysis of the chemical composition with a typical lateral

resolution of a micrometer and a typical depth resolution of a few tenths of a micrometer. Due to the relatively easy handling, SEM has found a wide range of applications in materials research, materials development, failure analysis, and quality control. There are several excellent monographs available on physical fundamentals, instrumental details, and applications of the scanning electron microscope (Ref 1–5). A short outline of beam/sample interactions, the basic instrumental design, the different types of contrast, SEM at elevated pressures, x-ray microanalysis, sample preparation, and a brief review of materials applications are presented in this article.

Beam/Sample Interactions

Interactions between the primary electrons and the sample result in a variety of signals that can be used for sample characterization (Table 1).

Backscattered Electrons. Elastic scattering (by single large-angle or multiple small-angle events) leads to a significant fraction of incident electrons that escape the sample. These electrons are termed backscattered electrons (BEs). The

BEs have energies up to the incident electron energy, with the energy distribution depending on the average atomic number of components in the sample. The fraction of incident electrons that leave the target is quantified by the backscattering coefficient (η), which again strongly depends on the atomic number (Fig. 1) and the angle between incident beam and sample surface (Fig. 2). Due to the strong dependence of η on the atomic number, BEs can be employed for imaging the differences in the mean atomic number of different constituents of a sample (compositional contrast). Backscattered electrons

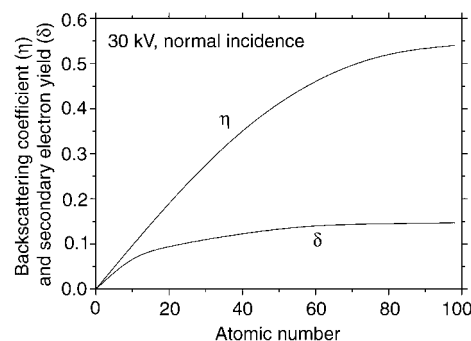


Fig. 1 Backscattering coefficient and secondary electron yield as functions of the atomic number at normal incidence

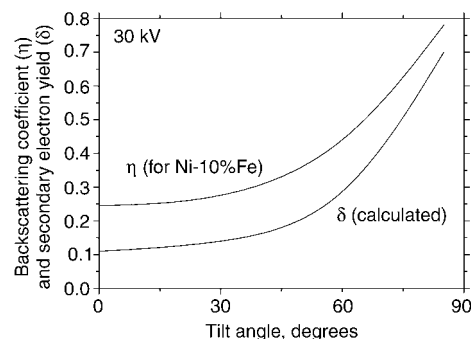


Fig. 2 Backscattering coefficient and secondary electron yield as functions of tilt angle (defined as the complement of the angle between primary beam and sample surface)

Table 1 Overview of contrast mechanisms, detectors, and typical lateral and depth resolution of signals used for imaging and analyzing materials in the scanning electron microscope

The lateral resolution and the depth of information are strongly dependent on primary electron energy and sample composition; typical values are shown.

Detected signal	Type of detector	Information	Lateral resolution	Depth of information
Secondary electrons	Scintillator/photomultiplier	Surface topography, compositional contrast	5–100 nm	5–50 nm
Backscattered electrons	Solid-state detector or scintillator/photomultiplier	Compositional contrast, surface topography, crystal orientation, magnetic domains	50–1000 nm	30–1000 nm
Specimen current	No external detector necessary	Complementary contrast to backscattered plus secondary electron signal	Same as backscattered electrons	Same as backscattered electrons
Characteristic x-rays (primary fluorescence)	Semiconductor detector (energy-dispersive) or crystal/proportional counter (wavelength-dispersive)	Element composition, element distribution	0.5–2 μm	0.1–1 μm
Cathodoluminescence	Photomultiplier	Detection of nonmetallic and semiconductive phases

may also be used to image the sample topography and the crystal orientation.

Secondary Electrons. Electrons that are produced as a result of interactions between the beam electrons and weakly bound conduction electrons of sample atoms are termed secondary electrons (SEs). The ratio of SEs to incident electrons is called secondary electron yield (δ). Because δ is almost independent of the atomic number (Fig. 1) but strongly depends on the angle between the incident beam and the sample surface (Fig. 2), SEs are mostly used to image the surface morphology (topographic contrast). Secondary electrons have much lower energies than BEs. The energy spectrum of SEs shows a pronounced maximum at approximately 3 eV; at approximately 50 eV, the frequency of SEs approaches 0. Therefore, all electrons leaving the sample with energies exceeding 50 eV are considered BEs. Secondary electrons are produced all along the way of the beam electrons through a sample. However, due to their low energy, only those SEs generated close to the surface can escape. The SEs generated by incident electrons entering the sample are called SE I; those generated by BEs when leaving the sample are called SE II. Because the number of SE II generated in a sample strongly depends on the backscattering coefficient, the contrast achieved with SEs may also contain a significant component of compositional contrast.

Absorbed Current. Electrons that flow from the sample to ground contribute to the absorbed current, which is equal to the incident beam current minus the current lost by BEs and SEs. In contrast to BE and SE images, regions that emit a large number of electrons appear dark in the absorbed current image.

X-Rays. Bombardment with electrons of sufficient energy leads to inner-shell ionization, and the target atoms are left in an excited state. Relaxation to the ground state occurs after approximately 10^{-12} seconds and results in the emission of either characteristic x-rays or Auger electrons. Because the energy of the characteristic x-rays depends on the atomic number (Moseley's law), the chemical composition of a sample can be determined from the characteristic x-ray lines. The probability that inner-shell ionization is followed by x-ray emission (rather than the Auger electron emission) is called fluorescence yield. This probability increases rapidly with increasing atomic number. In addition to the characteristic x-ray lines, a continuous spectrum from zero energy up to the energy of the incident beam is excited. The continuum x-rays (also termed bremsstrahlung) originate from the deceleration of the beam electrons in the Coulombic field of an atom. Because the characteristic x-ray lines must be measured against the continuous background, the bremsstrahlung often limits the detection of minor or trace components in a sample. Characteristic x-rays may be excited by the beam electrons (primary fluorescence) or by characteristic x-rays or bremsstrahlung generated in the sample (secondary fluorescence).

Cathodoluminescence. Electron bombardment may lead, in some samples, to the emission of long-wave radiation (in the ultraviolet and visible region of the spectrum) by a process known as cathodoluminescence (CL), which results from the recombination of electron-hole pairs created by the primary electron beam. Compared to imaging with BEs, SEs, or characteristic x-rays, CL finds only limited use in materials investigations.

Phonons. The major fraction of energy deposited in a sample is transferred to heat, that is, to lattice oscillations (phonons). The temperature rise in a sample is directly proportional to the incident electron energy and the beam current, and inversely proportional to the thermal conductivity of a sample and the beam diameter. For metals, the temperature rise is negligible under normal operation conditions. In materials of low thermal conductivity (e.g., ceramics, minerals), however, the temperature rise may be so high that volatile components (e.g., sodium, sulfur) are lost during investigation.

Interaction Volume. For the processes discussed previously, the sample volume in which the incident beam interacts with the material is illustrated in Fig. 3 for a sample consisting of Ni-10%Fe ($E_0 = 20$ keV, normal incidence). The distance traveled by an electron in a sample is called the electron range. According to Ref 6, the maximum electron range, R_{K-O} (micrometers), can be estimated from the following equation:

$$R_{K-O} = \frac{0.0276 \cdot A \cdot E_0^{1.67}}{\phi \cdot Z^{0.889}}$$

where A is the atomic weight (grams/mole), E_0 is the incident electron energy (kiloelectron volts), ϕ is the density (grams/cubic centimeters), and Z is the atomic number. Therefore, the interaction volume for primary electrons can be approximated as a hemisphere with radius R_{K-O} , while the sampling volume of BEs may be approximated as a disk with a diameter equal to $2R_{K-O}$ and a height of $0.3R_{K-O}$ (Fig. 3). Secondary electrons have a much smaller depth of information. According to Ref 7, the maximum depth of emission of SEs is on the order of 5 nm for metals (and up to 50 nm for insulators). Thus, the sampling volume of SEs is shown in Fig. 3 as a disk with a diameter equal to $2R_{K-O}$ and a height of 5 nm. The lateral resolution achievable with BEs is inferior compared to SEs, because the majority of the latter leaves the sample closer to the point of impact of the primary electrons.

The maximum x-ray generation range, R_X (micrometers), can be obtained from the maximum electron range, because characteristic x-rays can only be excited within the envelope containing electron energies above the critical ionization energy, E_c . The maximum x-ray generation range is, therefore, given by the following equation (Ref 1):

$$R_X = \frac{0.0276 \cdot A}{\phi \cdot Z^{0.889}} \cdot (E_0^{1.67} - E_c^{1.67})$$

The maximum x-ray generation range of Ni- K_{α} and Ni- L_{α} is shown in Fig. 3. Because the critical ionization energy is lower for the L-shell (0.854 keV) than for the K-shell (8.332 keV), R_X is smaller for Ni- K_{α} than for Ni- L_{α} . However, because absorption of the Ni- L_{α} line in nickel is much stronger than for the Ni- K_{α} line, the sampling volume for Ni- L_{α} radiation is smaller than for Ni- K_{α} radiation.

The x-ray generation range given previously considers only x-ray generation by beam electrons (primary fluorescence). Radiation excited by secondary fluorescence may originate in a much larger volume than the interaction volume of the electrons. Therefore, the spatial resolution of x-ray microanalysis may be strongly degraded in unfavorable cases. In the case of a Ni-10%Fe alloy, secondary fluorescence of Fe K_{α} by Ni K_{α} may take place in a distance up to approximately 55 μm away from the location of the original generation of the Ni K_{α} radiation (Fig. 3).

Basic Design of the Scanning Electron Microscope

The main components of the scanning electron microscope include the electron gun, probe-forming column (consisting of magnetic electron lenses, apertures, and scanning coils), electron detectors, and vacuum system (Fig. 4).

Electron Gun. Electrons are generated by thermionic emission or by an electric field. These electrons are then accelerated toward the sample. The most common type of electron gun consists of a tungsten filament that acts as a cathode. The anode consists of a grounded plate with a hole to let the electrons pass. The accelerating voltage is usually varied between 1 and 50 kV. A third electrode (Wehnelt cylinder) with a negative bias of a few hundred volts (relative to the cathode) is introduced to limit the emitting area to the tip of the tungsten filament. Lanthanum

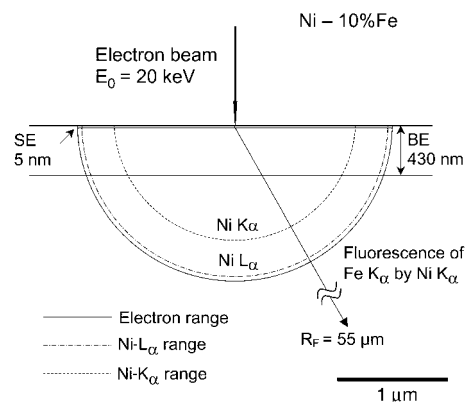


Fig. 3 Schematic illustration of the interactions between the electron beam and a sample (Ni-10%Fe alloy). Displayed are the electron range, the sampling depths of backscattered electrons (BE) and secondary electrons (SE), the x-ray generation ranges for Ni- K_{α} and Ni- L_{α} , and the range of fluorescence radiation, R_F , for Fe K_{α} excited by Ni- K_{α} .

hexaboride (LaB_6) cathodes are used in order to obtain a higher brightness, which has additional benefits, such as improving the lateral resolution. Field emission sources, with still higher brightness than the LaB_6 cathode, recently became available for routine operation in commercial instruments.

Lenses and Scanning Systems. Magnetic electron lenses are used to demagnify the image of the electron source (cross over) to the final spot size on the sample surface. In most cases, three lenses are used to obtain the required demagnification. Apertures are placed between the lenses to limit the beam diameter. In order to scan the electron beam across the sample, two sets of scanning coils are placed in the bore of the objective lens. The magnification is varied by changing the size of the area scanned on a sample. The electron beam scans the sample in much the same way as in a cathode ray tube (CRT) used for image formation on a television screen, and the output of the electron detectors is displayed on the screen of a synchronously scanned CRT. In modern instruments, the analog scanning systems are replaced by digital systems in which the movements of the beam on a sample are controlled with a computer. The analog signal from the electron detectors is digitized and stored as a number for each pixel.

Vacuum System. The electron gun and the column must be evacuated in order to avoid damage to the electron source and high-voltage breakdown in the gun. High vacuum is also necessary to minimize scattering of the electrons during their travel from the gun to the sample surface. In general, the vacuum system consists of a high-vacuum pump (oil-diffusion pump, turbomolecular pump, or ion pump) and a mechanical rotary pump. Operation of a tungsten filament requires a vacuum in the gun better than $\approx 10^{-3}$ Pa, a LaB_6 cathode better than $\approx 10^{-5}$ Pa, and a thermal field emitter better than $\approx 10^{-7}$ Pa. The high vacuum in the instrument leads to evaporation of volatile compounds, especially under electron bombardment, and sample characterization may be limited by the stability of the material. Recently, environmental SEM (Ref 8) has become a routine technique. In these instruments, pressures up to 2600 Pa are possible in the sample chamber during imaging with SEs and BEs. Due to multiple pressure-limiting apertures, a high vacuum can be retained at the same time in the electron gun and the column. The relatively high pressures in the sample chamber enable the study of fragile materials such as biological tissue, plastics, and grease. It is even possible to stabilize liquid water during electron microscopical investigation.

Detectors. The electron detector most commonly used in SEM is the Everhart-Thornley detector (Ref 9), which consists of a scintillator that, under electron bombardment, produces photons. The photons are converted to an electrical signal by means of a photomultiplier. The Everhart-Thornley detector can be used for SEs and BEs. However, there are more dedicated BE detectors, including large-area scintillator detec-

tors, BE-to-SE conversion detectors, or solid-state diode detectors. The latter may be divided into sectors in order to obtain different contrast by combining the output of the individual sectors in different ways (see the following). In environmental SEM, special SE and BE detectors (gaseous SE detector and gaseous BE detector), which use gas ionization to detect and amplify the signal, are necessary.

In addition to the main components of a scanning electron microscope described previously, most instruments are equipped with an energy-dispersive x-ray detector (silicon or germanium solid-state detector). Energy-dispersive x-ray spectroscopy enables the qualitative and quantitative chemical analysis of elements with an atomic number ≥ 5 (boron). x-ray detection may also be carried out by wavelength-dispersive spectrometers, which consist of a crystal to reflect only radiation of a certain wavelength (Bragg's law) and a proportional counter for x-ray detection.

Additional detectors that may be fitted to a scanning electron microscope include a cathodoluminescence detector (photomultiplier) and acoustic or infrared detectors. No special detector is needed for registration of the absorbed current, because the sample itself acts as detector.

Types of Contrast

The contrast, C , is defined as follows:

$$C = \frac{(S_2 - S_1)}{S_2} \quad S_2 > S_1$$

with S_1 and S_2 being the signals detected at two different locations in an image. By this definition, the contrast is restricted to values between 0 and 1 (or to 0 and 100%, if multiplied by a factor of 100).

Topographic Contrast. Secondary and backscattered electrons may be used to image the sample topography. Advantages in comparison to light optical microscopy include the greater depth of field and the higher lateral resolution. Topographic contrast is, in most cases, achieved with SEs. The topographic contrast in SE images results from the strong dependence of the SE yield on the tilt angle (Fig. 2), which is defined as the complement of the angle between the primary beam and the sample surface. The resulting contrast is analogous to an optical image in which the light comes from the detector and the observation direction is that of the incident electron beam. The three-dimensional impression in SE images is not only a result of the large depth of field but is also caused by the fact that the Everhart-Thornley detector attracts SEs from regions hidden from the detector (e.g., the far side of a sample or from inside cavities). At an edge, more SEs can exit the specimen, leading to a bright appearance of this feature (edge effect). The lateral resolution achievable with SEs mainly depends on the beam diameter and can

be as low as a few nanometers in favorable cases. Typical SE images with pronounced topographic contrast are shown in Fig. 5 (a-c) and 6(a) (see also Fig. 14a, 15b, 18a, 19a, and 20).

The topographic contrast in BE images is caused by the strong dependence of the backscattering coefficient on the tilt angle (Fig. 2). In addition, pronounced shadowing effects may contribute to the topographic contrast when the detector is located to one side of the specimen (as it is in the case for the Everhart-Thornley detector). The shadowing effects result from the fact that BEs are not attracted to the detector (in contrast to SEs), due to their high energies. However, if a solid-state diode detector is used, which is divided into sectors, or if several diodes are placed in an instrument (as is the case in some commercial electron microprobes), the topographic contrast can be enhanced by using the difference in the signal of opposite sectors of one detector or two detectors placed on opposite sides of the sample, respectively. Lateral resolution with BEs is inferior compared to SEs, because BEs generally travel larger distances within a sample.

Compositional (Material) Contrast. The increase of the backscattering coefficient with increasing atomic number (Fig. 1) forms the basis for the compositional contrast. Areas with higher atomic number (or mean atomic number for compounds) appear brighter in the BE image than areas with lower atomic number. The atomic number (Z) dependence of the backscattering coefficient (η) can be fitted with the following equation (Ref 10):

$$\eta = -0.025 + 0.016Z - 1.86 \times 10^{-4} Z^2 + 8.3 \times 10^{-7} Z^3$$

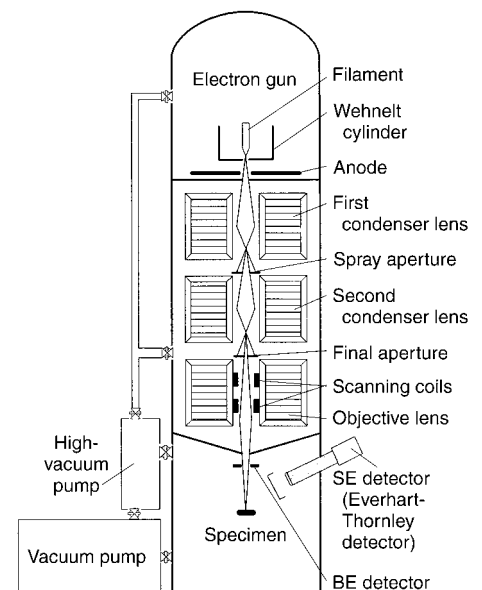


Fig. 4 Typical design (schematic) of a scanning electron microscope for secondary and backscattered electron imaging. SE, secondary electron; BE, backscattered electron

This equation is quite useful for estimating the backscattering coefficient of compounds. However, it should be kept in mind that there are local deviations from the general increase that are not represented by the preceding equation. For example, the backscattering coefficient of cobalt ($Z = 27$) is higher than that of nickel ($Z = 28$). Because the slope of the η -versus- Z curve decreases with increasing Z (Fig. 1), compositional contrast is more pronounced in the lower range of atomic numbers. For illustration, the compositional contrast of pairs of elements separated by one atomic number is 14% for boron-carbon, 6.7% for aluminum-silicon, and 0.41% for gold-platinum (Ref 1). In order to minimize influences of topographic contrast, the specimen should be flat and well polished for compositional imaging. Compositional contrast is useful for qualitative identification of phases and is especially suitable for qualitative evaluation of microstructural geometry by image analysis. Figures 5(d) and 6(b) and (c) show examples of compositional contrast obtained with BEs, with Fig. 6(b) demonstrating the superposition of topographic contrast.

Electron Channeling Pattern and Orientation Contrast. Based on an observation of a pattern of lines superimposed on the topographic BE image dating back to 1967, a number of techniques developed, yielding information on the crystal orientation, crystal structure, and defect density and allowing new types of imaging with the scanning electron microscope (SEM) (Ref 11–16). These techniques use the fact that the proportion of primary electrons backscattered and reaching the BE detector depends on the angle between the primary beam and the lattice planes. If the beam is parallel to certain crystallographic directions, the electrons follow the “channels” between densely packed planes and travel to a depth from which the probability of their reescape is small. Dark lines, forming patterns similar to Kikuchi lines in the transmission electron microscope, are thus formed (Fig. 7). When the direction of the primary beam deviates from these channeling directions, the proportion of electrons backscattered initially increases rapidly and then gradually with increasing angle of deviation.

There are several modes of SEM operation that use this effect (Ref 11–16):

- *Electron channeling patterns (ECPs):* At small magnifications (approximately $20\times$), the electron beam scans a large specimen area (approximately 5 mm, or 0.2 in., square), over which the angle of the incident beam varies by approximately 12° . In coarse-grained materials, each grain shows a line pattern from which the orientation of the grain can be determined with reference to the angle of the primary beam or to neighboring grains. This technique is also called electron backscatter diffraction or backscatter Kikuchi diffraction.
- *Selected-area channeling pattern (SACP):* When the point mode is used and the crystal size is larger than the beam (20 to 50 μm),

the crystal orientation can be precisely assessed (to approximately 1°) as follows. The cross-over point of the electron beam (under normal operating conditions, located at the last lens) is lowered to the specimen surface by adjusting the lens current, and the beam is tilted about this point by 5 to 15° , depending on the working distance. A typical pattern, called SACP, is obtained that is compared to standard patterns available for a number of materials (copper, steels, superalloys, silicon, and carbon, among others) or is indexed by commercially available computer software.

- *The step mode:* The SACP can be produced at small distances across the specimen surface by using the step mode. Every significant change of the pattern indicates a grain boundary. In contrast to most other methods (e.g., light microscopy of etched surfaces), even twin boundaries or small-angle boundaries are safely detected. By automated registration

and analysis, a map of the grain-boundary structure or a gray-level image of the grains (similar to an image obtained for some materials in polarized light) can be generated. Software for this technique (Ref 11) is available commercially under the term *orientation imaging microscopy*.

- *Electron channeling contrast imaging (ECCI):* The SEM is operated at higher magnifications (200 to $5000\times$) in the ECP mode. Tilting of the beam across the field of view is negligible at these magnifications, and the dependence of BE intensity on crystal orientation causes a contrast between individual crystals. Furthermore, similar contrast effects as in transmission electron microscopy are observed by concentrations of lattice defects, dislocation clusters, and subgrain boundaries. Persistent slide bands in a single crystal of copper and dislocation networks in porous materials undergoing cyclic deformation have

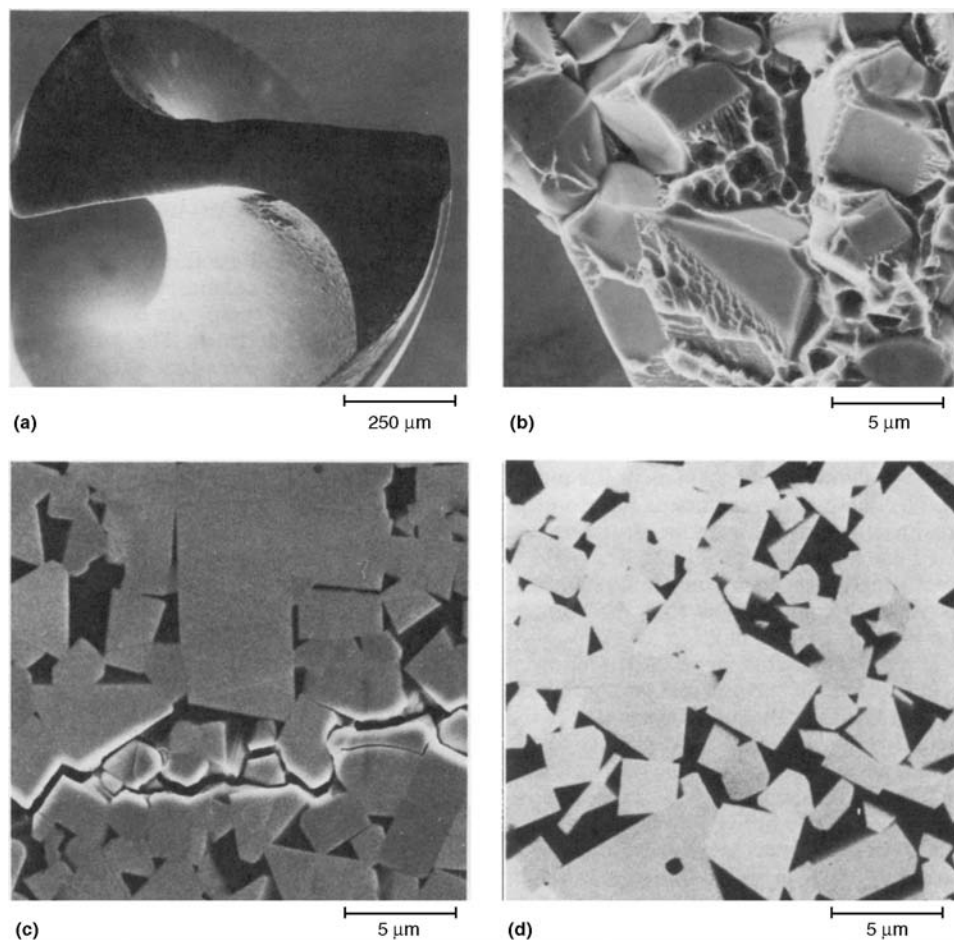


Fig. 5 Typical scanning electron micrographs of a sintered WC-12Co cemented carbide (hard metal used in metal cutting operations). (a) Secondary electron image of the surface of a worn drill (strong topographic contrast). $60\times$. (b) Secondary electron image of the fracture surface in a fracture toughness test specimen (strong topographic contrast). $3000\times$. (c) Secondary electron image of a plane section through a cracked region showing weak orientation contrast between the hexagonal carbide crystals and strong material contrast between the carbide and the binder (darker due to the lower atomic number). The crack edges appear bright due to the pronounced edge effect. $3000\times$. (d) Back-scattered electron image (primary electron energy, 15 keV) of a plane section showing strong compositional contrast between tungsten carbide (light) and the cobalt binder phase (black). In addition, some orientation contrast exists for the different tungsten carbide crystals. $3000\times$